RSC Advances

PAPER

View Article Online
View Journal | View Issue

Cite this: *RSC Adv.*, 2025, **15**, 28984

Core–shell TiO_2@Co_3O_4 anode materials with *in situ* formed nanoscale Co-based interfaces for enhanced lithium-ion transport

Yuan Chen,[abc] Hao Li,[abc] Huawei Luo,[abc] Li Chen,[abc] Yi Yang,[abc] Marie-Christine Record,[d] Pascal Boulet,[d] Juan Wang,[abc] Jan-Michael Albina[abc] and Weiliang Ma *[abc]

In this study, TiO_2@Co_3O_4 microspheres with a core–shell structure are successfully synthesized *via* a homogeneous precipitation method. The composition, structure, and micro-morphology of the prepared microspheres are systematically characterized. The results confirm that spinel Co_3O_4 uniformly coats the surface of anatase TiO_2 microspheres, forming a lychee-like morphology with excellent dispersibility. The TiO_2@Co_3O_4 anode material exhibits significantly improved cycling performance, specific capacity, cycling stability, and rate capability compared to commercial graphite. To further investigate the synergistic interaction between TiO_2 and Co_3O_4, *ex situ* characterization, cyclic voltammetry, electrochemical impedance spectroscopy, and theoretical calculations are conducted. In contrast to the layered distribution observed prior to cycling, Co is redistributed in the form of nanoscale CoO and metallic Co particles dispersed across the TiO_2 after cycling, and form a stable interface. Due to interfacial electron accumulation, Ti and Co adopt a higher oxidation state, leading to stronger electron binding. This phenomenon reduces the electrostatic interaction between lithium ions and the surrounding charge, facilitating lithium-ion intercalation/deintercalation and lowering electrode impedance.

Received 24th June 2025
Accepted 30th July 2025

DOI: 10.1039/d5ra04485e

rsc.li/rsc-advances

1 Introduction

As intermittent green energy sources, such as wind and solar power, become more widely adopted, alongside the rapid expansion of the electric vehicle industry, the demand for enhanced performance, longevity, and safety in energy storage technologies has risen significantly.[1,2] Lithium-ion batteries (LIBs), the most widely used secondary batteries, have attracted significant attention due to their high energy density, long cycle life, and low self-discharge rate.[3–5] In LIBs, anode materials play a pivotal role in facilitating the intercalation and deintercalation of lithium ions, thereby enabling the charging and discharging processes. The performance of anode materials directly determines key battery metrics, including specific capacity, cycle life, rate capability, and safety.[2,6]

Compared with common carbon-based materials,[7,8] alloy materials,[9,10] and various composite materials,[11,12] polycrystalline TiO_2 exhibits minimal volume changes during the intercalation and deintercalation of lithium ions, resulting in excellent cycling stability.[13] However, its applications are constrained by a wide bandgap, low electrical conductivity, and slow lithium-ion transport kinetics.[14,15] Current efforts to optimize TiO_2 anode materials primarily focus on nanostructuring[16] and composite formation.[17,18] Nanostructured TiO_2 anodes significantly enhance the contact area between the material and the electrolyte, increase lithium-ion transport channels, and provide more lithium-ion storage sites, thereby improving their electrochemical performance.[19–22] Due to high energy density, transition metal oxides, Mn_2O_3,[23] Fe_2O_3,[11] Fe_3O_4,[24] CuO,[25] NiO,[26] and Co_3O_4,[27] are potential candidates to form composites with TiO_2.

Common morphologies of TiO_2-based composite materials include spherical particles, nanoparticles, nanorods, nanofibers, nanotubes, nanobelts, nanosheets, and three-dimensional (3D) array structures. Each morphology imparts distinct electrochemical advantages to the material: spherical structures are beneficial for enhancing packing density and cycling stability;[28] nanoparticles offer high specific surface area and short ion diffusion paths, making them suitable for high-rate applications;[29] one-dimensional structures such as rods,

[a]*Hubei Provincial Key Laboratory of Green Materials for Light Industry, Collaborative Innovation Center of Green Light-Weight Materials and Processing, School of Materials and Chemical Engineering, Hubei University of Technology, Wuhan 430068, China. E-mail: maweiliang@hbut.edu.cn*

[b]*New Materials and Green Manufacturing Talent Introduction and Innovation Demonstration Base, Wuhan 430068, China*

[c]*Laboratory of Artifiacial Quantum 2D Materials, Hubei University of Technology, Wuhan 430068, China*

[d]*Aix-Marseille University, IM2NP, CEDEX 20, 13397 Marseille, France*

Fig. 1 Schematic diagram of preparation of TiO_2@Co_3O_4 microspheres.

fibers, and tubes provide continuous electron transport pathways and effectively buffer volume expansion-particularly, hollow tubular structures exhibit excellent structural stability;[30,31] nanobelts and nanosheets offer large surface areas and rapid charge transport capabilities;[32,33] while 3D array structures improve overall electrode conductivity and interfacial stability.[34,35]

Co_3O_4 reacts with lithium ions to form lithium cobalt oxides and other compounds, enabling lithium-ion storage and release,[36] and providing high energy density of 890 mA h g^{-1}.[37] However, the redox reactions of Co_3O_4 during cycling result in continuous phase transformations, causing significant volumetric effects that reduce its cycling stability and the reversibility of redox reactions.[37] Studies indicate that TiO_2 and Co_3O_4 exhibit synergistic effects, whereby the structural stability and excellent cycling performance of TiO_2, combined with the high specific capacity of Co_3O_4, allow the synthesis of composite materials that integrate the advantages of both.[36,38–40] Most studies have focused on the reactions and high specific capacity of Co_3O_4; however, the interaction between Co_3O_4 and partially coated composite materials raises questions about its actual contribution to battery performance. The underlying mechanisms of the synergistic effects in such composites remain unclear.

In this study, TiO_2 microspheres were used as precursors, and Co_3O_4 was coated on the surface of TiO_2 microspheres *via* a homogeneous precipitation method. The preparation process of TiO_2@Co_3O_4 microspheres is illustrated in Fig. 1. The composition, structure, and micro-morphology of both TiO_2 and TiO_2@Co_3O_4 microspheres were characterized, and their charge–discharge performance, cycling stability, and rate performance were evaluated. Furthermore, density functional theory (DFT) calculations and electrochemical performance analyses were conducted to compare the material properties before and after coating, revealing the synergistic mechanisms between TiO_2 and Co_3O_4. This study provides new insights and methodologies for the design and optimization of lithium-ion battery anode materials.

2 Results

2.1 Phase and morphology

The uncalcined TiO_2 microspheres and cobalt carbonate-coated TiO_2 microspheres were both amorphous (Fig. 2a and S1). After calcination, diffraction peaks corresponding to anatase TiO_2 (ref. 03-065-5714) and spinel Co_3O_4 (ref. 00-043-1003) appeared in the samples, without obvious other impurities peaks. The lattice constants of anatase-phase TiO_2 are a, b = 3.780 Å, c = 9.515 Å, while those of spinel Co_3O_4 are a, b, c = 8.08 Å. This phase structure was further validated by the Raman spectra of TiO_2@Co_3O_4 microspheres (Fig. 2b). The spectrum revealed characteristic vibrational peaks of anatase TiO_2 at Eg(1) (142 cm^{-1}), B1g (394 cm^{-1}), A1g (252 cm^{-1}), and Eg(2) (634 cm^{-1}),[41] as well as peaks associated with spinel Co_3O_4 at F2g (193 cm^{-1}), Eg (477 cm^{-1}), F2g (517 cm^{-1}), F2g (613 cm^{-1}), and A1g (684 cm^{-1}).[42,43]

Surface morphology observations revealed that the anatase TiO_2 microspheres exhibit excellent monodispersity, smooth surfaces, and small pores. The range of particle size is 500 nm to 800 nm, with an average size of 687.4 nm (Fig. 2c, d, S2 and S4). After 4 h of calcination, some TiO_2 microspheres in the TiO_2@Co_3O_4 sample showed pore closure, with Co_3O_4 uniformly coating the surface of TiO_2 microspheres to form

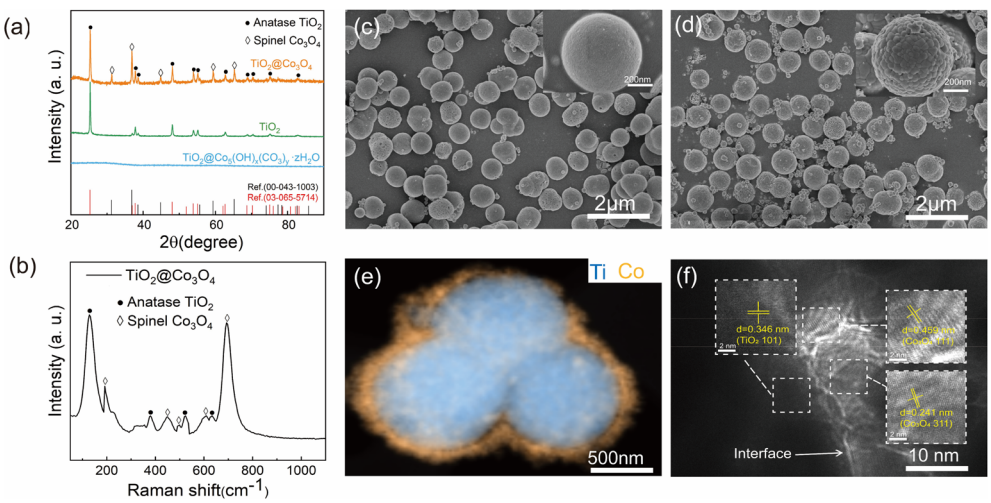

Fig. 2 (a) XRD pattern; (b) Raman spectra of TiO_2@Co_3O_4 microspheres; (c) morphology of TiO_2 after calcination at 600 °C for 4 h; (d) morphology of TiO_2@Co_3O_4 after calcination at 850 °C for 4 h; (e) TEM morphology and elements mapping of calcined TiO_2@Co_3O_4; (f) interface between TiO_2 and Co_3O_4 of TiO_2@Co_3O_4 microspheres.

lychee-like microspheres. These microspheres exhibited uniform sizes, regular shapes, good monodispersity, and undamaged surfaces. The surface texture and pore structures facilitate the intercalation and deintercalation of lithium ions. However, when the calcination time was extended to 8 h, the microsphere size increased to approximately 2 μm to 3 μm, with excessive grain growth inside (Fig. S3), resulting in uneven grain size distribution, overfilled interparticle pores, and noticeable aggregation.

To gain deeper insights into the microstructure of the composites, transmission electron microscopy (TEM) was performed, as shown in Fig. 2e and f, together with elemental mapping. The high-resolution transmission electron microscopy (HRTEM) image of the TiO_2@Co_3O_4 microsphere interface (Fig. 2f) reveals that a uniform Co_3O_4 layer with a thickness of approximately 100 nm is attached to the surface of the TiO_2 microsphere and forms a stable interface with the TiO_2 substrate. This observation indicates that the amorphous Co_3O_4 precursor transformed into a crystalline structure upon calcination, which is consistent with the XRD analysis.

2.2 Battery performance analysis

2.2.1 Charge–discharge tests. The charge–discharge tests for lithium-ion batteries were conducted at a current density of 0.2 C to prevent accelerated side reactions, such as electrolyte decomposition or lithium metal deposition, under high-rate conditions. This ensured the accuracy, safety, and standardization of the tests. The first discharge and charge profiles of anatase TiO_2 exhibited distinct plateaus at 1.75 V and 2.0 V, respectively (Fig. 3a). During the initial cycle, the battery demonstrated an initial discharge-specific capacity of 323.9 mA h g^{-1} and a charge-specific capacity of 155.6 mA h g^{-1}, corresponding to an initial coulombic efficiency of 48.0%. These results indicate a significant irreversible capacity loss in the first discharge, where lithium ions intercalated into the material were not fully extracted in the subsequent charge. Under the same testing conditions, the charge–discharge profiles of Co_3O_4 anodes are shown in Fig. S5, where the first discharge and charge curve reveals a prominent plateau at approximately 1.2 V and 2.0 V, and Co_3O_4 delivers a high discharge-specific capacity of approximately 508.9 mA h g^{-1} and a charge-specific capacity of 765.9 mA h g^{-1}, resulting in an initial coulombic efficiency of 86.9%. In subsequent cycles, the discharge and charge plateaus gradually shift and become smoother, indicating partial structural reconstruction and increased reversibility.

TiO_2@Co_3O_4 anodes (Fig. 3b) exhibited discharge and charge plateaus at 1.75 V and 2.0 V, corresponding to lithium-ion intercalation and deintercalation at octahedral sites in anatase TiO_2. Additionally, stable plateaus were observed between 1.0 V to 1.5 V. During the initial cycle, TiO_2@Co_3O_4 demonstrated an exceptionally high initial discharge-specific capacity of 713.1 mA h g^{-1}. The initial charge–discharge specific capacities were 713.1 mA h g^{-1} and 619.0 mA h g^{-1}, respectively, with a coulombic efficiency of 86.8%. The reversible capacity, defined as the capacity that can be utilized repeatedly during charge–discharge cycles, was 619.0 mA h g^{-1}. After 2, 3, 10, and 100 cycles, the reversible capacities of TiO_2@Co_3O_4 were 564.6 mA h g^{-1}, 555.0 mA h g^{-1}, 495.0 mA h g^{-1}, and 482.0 mA h g^{-1}, respectively. These values significantly exceeded those of anatase TiO_2 anodes, which were

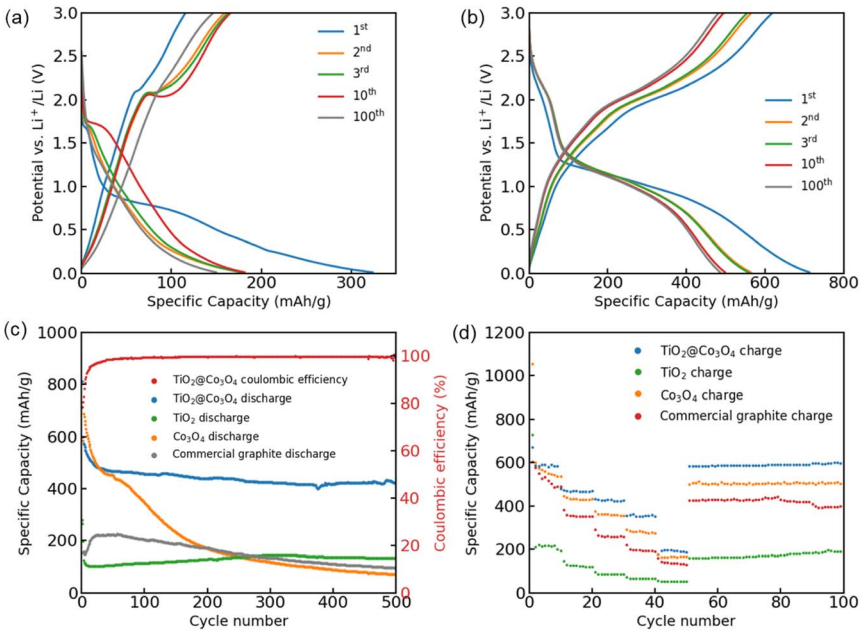

Fig. 3 Charge and discharge curves of anatase TiO_2 (a) and TiO_2@Co_3O_4 (b) for 1, 2, 3, 10, and 100 cycles at a 0.2 C current density; (c) cyclic performance of anatase TiO_2, TiO_2@Co_3O_4, spinel Co_3O_4, and commercial graphite at a 2 C current density, with the coulombic efficiency diagram of TiO_2@Co_3O_4; (d) rate performance of anatase TiO_2, TiO_2@Co_3O_4, spinel Co_3O_4, and commercial graphite at current densities of 100 mA g^{-1}, 200 mA g^{-1}, 400 mA g^{-1}, 800 mA g^{-1}, and 1600 mA g^{-1}.

158.6 mA h g^{-1}, 162.7 mA h g^{-1}, 165.7 mA h g^{-1}, and 146.6 mA h g^{-1}, respectively. After 100 cycles, TiO_2@Co_3O_4 exhibited a capacity improvement of 228.8%. TiO_2@Co_3O_4 demonstrated extended voltage plateaus, particularly below 1 V, with enhanced charge–discharge stability.

2.2.2 Cycling performance. To further evaluate the cycling performance of different materials, half-cells using anatase TiO_2, spinel Co_3O_4, TiO_2@Co_3O_4, and commercial graphite as anodes were tested at a current density of 2C for 500 cycles. The discharge-specific capacities are shown in Fig. 3c. After 500 cycles, the reversible capacities of anatase TiO_2 and TiO_2@Co_3O_4 anodes were 132.3 mA h g^{-1} and 425.6 mA h g^{-1}, respectively, representing a 221.5% improvement for TiO_2@Co_3O_4. This indicates that the coated TiO_2@Co_3O_4 anode exhibited significantly enhanced capacity even after enduring high current densities and prolonged cycling. Anatase TiO_2 demonstrated a relatively low initial capacity but excellent cycling stability, with minimal capacity degradation, highlighting its inherent stability and suitability for combination with high-capacity materials. In contrast, spinel Co_3O_4 exhibited a high initial specific capacity (731.3 mA h g^{-1}), but its capacity rapidly declined with increasing cycles. After 500 cycles, the reversible capacity of Co_3O_4 was only 71.4 mA h g^{-1}, indicating structural instability during lithium-ion intercalation/deintercalation, leading to volume expansion, material fracture, and deactivation. Commercial graphite exhibited moderate capacity with excellent cycling stability, showing minimal capacity loss over multiple cycles.[43] The capacity of commercial graphite is around 200 mA h g^{-1} after 500 cycles, wchih is relatively high compared to ref. 44. To check the side effects during the cycling, voltage profile of each anode are provide in Fig. S6. For the graphite electrode, the voltage profile still shows the typical plateau below 0.2 V, consistent with the Li^+ intercalation/deintercalation process of commercial graphite, as reported in the literature,[45] indicating no obvious side effects. After 500 cycles, the coulombic efficiency of TiO_2@Co_3O_4 remained at 99.8%, demonstrating its high reversibility, excellent power output capability, rapid charge–discharge capability, and stable capacity retention. A solid electrolyte interphase (SEI) layer is typically attributed to surface reactions.[13,27] While the initial coulombic efficiency of TiO_2@Co_3O_4 is only modestly improved compared to TiO_2, and both values fall within typical ranges for metal oxide anodes. This modest improvement is unlikely to stem solely from changes in the SEI chemistry. More importantly, the TiO_2@Co_3O_4 electrode shows much better capacity retention and rate capability than both TiO_2 and Co_3O_4, suggesting that the enhancement is sustained during long-term cycling, which cannot be attributed solely to SEI formation in early cycles.

2.2.3 Rate performance. Rate performance tests at different charge–discharge rates (Fig. 3d) evaluated the reversible capacities of anatase TiO_2, TiO_2@Co_3O_4, spinel Co_3O_4, and commercial graphite at current densities of 100 mA g^{-1}, 200 mA g^{-1}, 400 mA g^{-1}, 800 mA g^{-1} and 1600 mA g^{-1}. The reversible capacities were as follows: 217.1 mA h g^{-1}, 125 mA h g^{-1}, 86.1 mA h g^{-1}, 65.6 mA h g^{-1} and 52.5 mA h g^{-1} for anatase TiO_2, 559.8 mA h g^{-1}, 432.8 mA h g^{-1}, 360.7 mA h g^{-1}, 283.1 mA h g^{-1} and 165.3 mA h g^{-1} for spinel Co_3O_4, 534.2 mA h g^{-1}, 352.1 mA h g^{-1}, 259.8 mA h g^{-1}, 195.5 mA h g^{-1} and 137.6 mA h g^{-1} for commercial graphite, and 590.8 mA h g^{-1}, 470.1 mA h g^{-1}, 429.4 mA h g^{-1}, 352.3 mA h g^{-1} and 196.1 mA h g^{-1} for TiO_2@Co_3O_4. For TiO_2@Co_3O_4, the initial specific capacity at 100 mA g^{-1} was approximately 600 mA h g^{-1}. As the rate increased, the specific capacity gradually decreased, with a significant drop at 1600 mA g^{-1}. However, when the current density returned to 100 mA g^{-1}, the capacity recovered to nearly 600 mA h g^{-1}, demonstrating excellent rate performance and reversibility. This indicates that high-rate charge–discharge cycles did not significantly compromise the structural integrity of the material.

3 Discussion

The enhancement of lithium-ion battery performance by anode materials primarily depends on the intercalation and deintercalation speed of Li^+ and the efficiency of lithium-ion migration within the anode material. During charge and discharge processes, Li^+ ions intercalate into the octahedral sites of anatase-phase TiO_2, forming a stable phase. The high symmetry of spinel Co_3O_4, with a ratio of 1 : 2 between tetrahedral and octahedral voids, theoretically provides abundant intercalation sites for Li^+, thereby improving the capacity of TiO_2@Co_3O_4 batteries.[46] The specific reaction of TiO_2 equations are provided in eqn (1), as well as the multi-step reduction of Co_3O_4 to Co^0 in eqn (2)–(4).[47]

$$TiO_2 + xLi^+ + xe^- \rightarrow Li_xTiO_2 \quad (1)$$

$$Co_3O_4 + 2Li^+ + 2e^- \rightarrow 3CoO + Li_2O \quad (2)$$

$$CoO + 2Li^+ + 2e^- \rightarrow Co + Li_2O \quad (3)$$

$$Co_3O_4 + 8Li^+ + 8e^- \rightarrow 4Li_2O + 3Co \quad (4)$$

A noticeable decline in the specific capacity of the TiO_2@Co_3O_4 electrode is observed during the first 30 charge–discharge cycles, after which the capacity gradually stabilizes beyond 100 cycles. This behavior indicates that irreversible structural transformations occur in the electrode during cycling. To investigate these changes, we disassembled the coin cells after 100 cycles at the end of the charge and discharge states, and performed *ex situ* characterizations.

As shown in Fig. 4a, the *ex situ* XRD patterns of the electrodes after 100 cycles reveal the absence of Co_3O_4 diffraction peaks. Instead, characteristic peaks corresponding to metallic Co and CoO are detected, which is consistent with the proposed electrochemical conversion reactions. The *ex situ* HRTEM image under the discharged state (Fig. 4b) shows that cobalt is partially present in the form of cobalt monoxide (CoO), with the (111) lattice plane clearly observed, having a *d*-spacing of 0.248 nm. Elemental mapping by EDX indicates that Co is dispersed in dot-like patterns on the TiO_2 matrix surface.

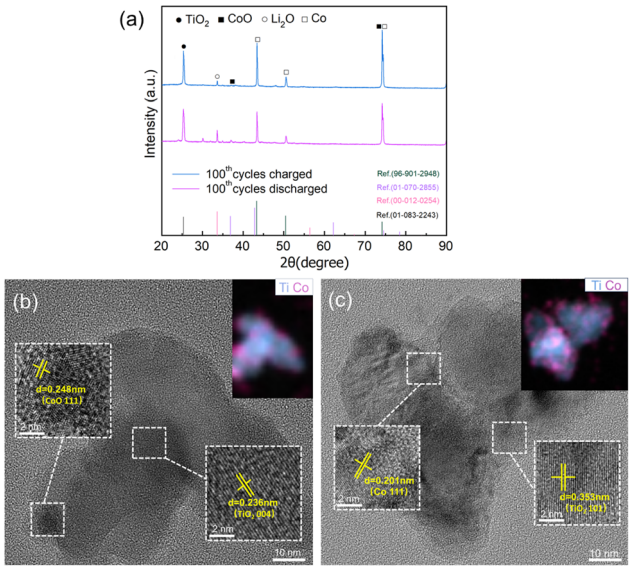

Fig. 4 *Ex situ* testing of active materials of the 100th cycle under 2 C: (a) XRD; (b) discharged HRTEM; (c) charged HRTEM.

In the charged state, the anatase TiO_2 structure, as evidenced by the (101) plane with an interplanar spacing of 0.353 nm. Meanwhile, Co remains present on the surface in large quantities, and its lattice spacing of 0.201 nm corresponds to the (111) plane of metallic Co. These results suggest that after prolonged cycling, the original nanoscale shell structure of Co_3O_4 breaks down. The initially continuous film-like coating transforms into discrete Co and CoO nanoparticles. Additionally, a small amount of Li_2O is present, although its detection is primarily inferred from XRD due to the low atomic weight of lithium. Following this structural transformation, the electrode enters a relatively stable state, as reflected in the stabilization of the specific capacity over continued cycling.

Based on the *ex situ* XRD, 4 heterojunctions were constructed from fully relaxed anatase TiO_2, Co_3O_4, CoO, Co and Li_2O (Fig. S7). The equilibrium lattice parameters of bulk structures are listed in Table S2.

Five-layers films (Fig. S9 and S10) were cleaved from the (101) high-energy plane of anatase TiO_2 and the (111) high-energy plane of spinel Co_3O_4, CoO, Co and Li_2O.[48,49] These layers are illustrated in Fig. 5a and b, along with the electron localization function (ELF). The lattice parameters of the TiO_2@Co_3O_4 heterojunction are $a = 11.280$ Å, $b = 10.280$ Å, and $c = 40$ Å. No significant lattice distortion was observed around the interface. ELF analysis revealed no electron accumulation along the Ti–O and Co–O bonds of TiO_2@Co_3O_4 and TiO_2@CoO; instead, electrons were localized around the ions, indicating the ionic nature of these bonds. Specifically, the electron behavior near the interface was consistent with that in the sub-junctions. The bonding states of Ti–O and Co–O of TiO_2@Co_3O_4 were confirmed by the positive integrated crystal orbital Hamilton population (ICOHP) values (Fig. S11), suggesting the formation of a stable heterojunction.

To elucidate the charge transfer behavior at the interface, we calculated the charge density difference in the interface models. The results show charge accumulation at the interface in all four models. To quantitatively evaluate the extent of charge transfer, we compared the Bader charges of atoms near the interface with those in the individual sub-junctions. The average Bader charges of Ti and Co atoms on either side of the TiO_2@Co_3O_4 interface are found to be 2.29+ and 1.50+, respectively, which are higher than those in the sub-junctions, where the charges are 2.24+ and 1.39+. This indicates an increase in the oxidation states of Ti and Co near the interface. If we separate the heterojunction into two parts by the interface, the amount of charge transferred across the interfaces of TiO_2@Co_3O_4, TiO_2@CoO, TiO_2@Co, and TiO_2@Li_2O are 8.90*e*, 3.04*e*, 1.82*e*, and 0.91 *e*, respectively. TiO_2@CoO exhibits greater charge transfer than TiO_2@Co, suggesting faster Li + insertion due to charge accumulation on the CoO side. As the reaction proceeds toward TiO_2@Co, the insertion becomes slower while delithiation becomes easier, contributing to the observed cycling behavior.

To further confirm the oxidation state variation, the high-resolution X-ray photoelectron spectroscopy (XPS) was conducted on the grown core–shell structures. As shown in Fig. 5e, the Co 2p region of Co_3O_4 (Fig. 5f) features four distinct peaks: two prominent main peaks and two satellite peaks. The main peaks correspond to Co $2p_{3/2}$ at 780 eV and Co $2p_{1/2}$ at 795 eV. For the TiO_2@Co_3O_4 structure, these peaks shift toward higher binding energies, consistent with our theoretical calculations. Fig. 5g and h present the Ti 2p spectra for TiO_2 and TiO_2@-Co_3O_4, respectively. In TiO_2, three peaks are observed, including two main peaks at 459.0 eV and 464.5 eV, corresponding to Ti $2p_{3/2}$ and Ti $2p_{1/2}$, as well as a satellite peak. After the formation of the composite, a noticeable shift in binding energy suggests an increased oxidation state of Ti, which is in line with the results from Bader charge analysis.

Cyclic voltammetry (CV) tests conducted with half-cells using TiO_2, TiO_2@Co_3O_4, and Co_3O_4 as anode materials are shown in Fig. 6a and b, and S12. For the TiO_2 electrode, the first scan exhibited a reduction peak at 1.7 V and an oxidation peak at 2.2 V, corresponding to the initial discharge and charge processes, respectively. These redox peaks are characteristic of the Li^+ intercalation/deintercalation reactions in anatase TiO_2, indicating good reversibility. The specific reaction equation is provided in eqn (2).[50,51] During the first scan, the current response was relatively low, suggesting limited electrochemical activity during the initial scan. However, a slight increase in current response was observed during the second scan, indicating that the electrode surface became more active after the initial cycle or that some degree of structural changes occurred in the material. As the current further increased during the third scan, it suggested that the electrochemical behavior of the electrode material had stabilized after multiple cycles. The subtle differences between the CV curves for different scans highlight the progressive activation of the electrode material. With increasing scan numbers, the current peaks gradually grew, implying that the activation process of the electrode material or changes in surface structure led to an enhanced reaction rate over time.

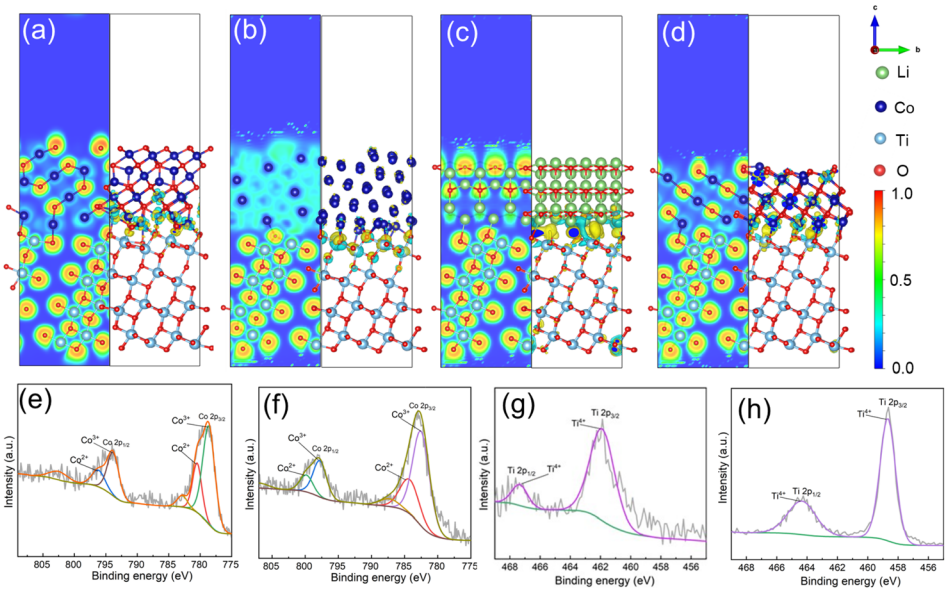

Fig. 5 The heterojunction model of TiO_2@Co_3O_4 (a), TiO_2@Co (b), TiO_2@Li_2O (c) and TiO_2@CoO (d). The displaying ELF map is illustrated on the left and the charge difference on the right, where the isosurface is set at 0.005 and marked by by positive (yellow) and negative (cyan) regions. To provide a details of the selected planes, the 3D figures of ELF figures are shown in Fig. S10. The XPS spectrum of Ti (e and f) and Co (g and h) before (e and g) and after cycling.

The CV curves of the TiO_2@Co_3O_4 material (Fig. 6b) not only exhibit the redox characteristics of anatase TiO_2 but also display a reduction peak at 1.0 V during the first scan, corresponding to the multi-step reduction of Co_3O_4 to Co^0. The specific reaction equations are provided in eqn (3)–(5). Additionally, the TiO_2@Co_3O_4 material exhibits higher current responses, indicating more intense electrochemical reactions under these experimental conditions. This suggests enhanced lithium-ion conductivity or improved electron transport properties. Notably, during the second and third scans, the current density

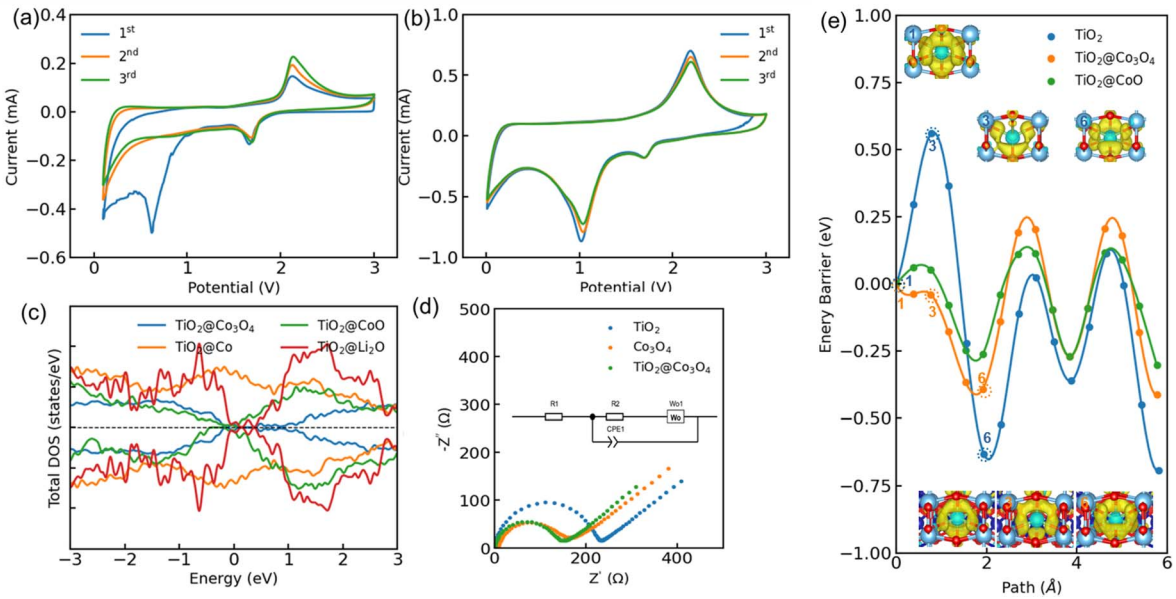

Fig. 6 CV curve of anatase TiO_2 (a) and TiO_2@Co_3O_4 (b) with a scanning speed of 0.3 mV s^{-1} and a voltage window of 0.01 V to 3.0 V; (c) total DOS of the films; (d) Nyquist plots of TiO_2, TiO_2@Co_3O_4, and Co_3O_4 in the frequency range of 1×10^{-2} Hz to 1×10^{6} Hz. The inset shows the equivalent circuit diagram, where CPE1 represents the double-layer capacitance, R_1 represents the internal resistance of the battery, R_2 represents the charge transfer resistance, and Wo_1 represents the Warburg coefficient for lithium-ion diffusion.[54] (e) Calculated lithium-ion migration energy barriers in TiO_2, TiO_2@Co_3O_4 and TiO_2@CoO along the migration path shown in Fig. S13. 6 inset figures illustrates the charge difference at sites 1, 3, and 6. The isosurface level is set to 0.005, with yellow indicating charge accumulation and cyan representing charge depletion.

increases significantly, suggesting progressive activation at the interface and a substantial enhancement in the Li^+ intercalation/deintercalation rate. The current variations observed over the three scans are relatively similar, indicating that the electrochemical behavior of the electrode material stabilizes after the second scan.

The activation of the anodes can be confirmed by the density of states(DOS) analysis. The calculated bandgap of thin-film TiO_2 is 2.47 eV (Fig. 6c), which is lower than the experimental value of 3.2 eV.[52] It should be noted that the generalized gradient approximation (GGA) functional cannot accurately describe the d-orbitals of transition metals, leading to an underestimation of bandgap widths. Typically, a Hubbard U correction is introduced to obtain more accurate bandgap values; however, an excessively high *U* value can distort the band structure. In this study, a moderate *U* value was adopted. Meanwhile, the calculated bandgap values of spinel Co_3O_4 are 1.08 eV, 0.31 eV, and 1.54 eV for bulk, thin film, and experimental measurements, respectively.[53] After forming the composite, the bandgap of $TiO_2@Co_3O_4$ decreases compared to that of pure TiO_2 (Fig. 6c). Compared to $TiO_2@Co_3O_4$, the density of states (DOS) of TiO_2@CoO indicates higher electronic conductivity, while TiO_2@Co exhibits metallic behavior. This suggests that the electrode material after cycling is expected to possess lower internal resistance.

The electrochemical impedance spectroscopy (EIS) results of anatase TiO_2, spinel Co_3O_4, and $TiO_2@Co_3O_4$ anodes are shown in Fig. 6d. Based on the lithium-ion intercalation and deintercalation mechanisms in the anodes, the equivalent circuit illustrated in the inset of Fig. 6d was used to fit the EIS spectra. The results show that the internal resistances of anatase TiO_2, spinel Co_3O_4, and $TiO_2@Co_3O_4$ are 23.81 Ʊ, 11.67 Ʊ, and 4.95 Ʊ, respectively, while the charge transfer resistances are 223.72 Ʊ, 186.21 Ʊ, and 161.41 Ʊ, respectively. The internal resistance of $TiO_2@Co_3O_4$ is significantly lower than those of the other two materials, and its conductivity is markedly higher. Under high-rate (rapid charge–discharge) conditions, batteries require rapid charge transfer, and lower charge transfer resistance contributes to maintaining high electrochemical reaction efficiency.

After lithium intercalation, lithium ions migrate inward from the interface along the octahedral interstitial channels of TiO_2 (Fig. S13), including 16 potential migration states. Lithium ions follow a pathway where electrons traverse the Ti–O bonds *via* a Ti–O–Ti–O conduction route to the next Ti–O bond, forming a continuous conductive path.[54] During migration, charge transfers from lithium ions to the bonding sites, and reducing Co and Ti. Conversely, during delithiation, these transition metals are reoxidized. For TiO_2 anodes, the initial lithium-ion migration exhibits an energy barrier of approximately 0.61 eV (Fig. 6e), and the barrier increases to around 0.8 eV within the anode. In contrast, the TiO_2@CoO presents a energy barrier of 0.28 eV, while the $TiO_2@Co_3O_4$ composite shows nearly no energy barrier at the initial migration stage, indicating easier lithium-ion transport through the surface layer. The internal energy barrier of the composite is approximately 0.6 eV, lower than that of TiO_2 and Co_3O_4 (Fig. S14).

Charge differential calculations (Fig. 6e) reveal significant charge fluctuations in the TiO_2 anode, particularly at sites 1 and 6, where charge shifts toward Ti atoms compared to site 3. In contrast, the $TiO_2@Co_3O_4$ composite exhibits more stable charge transfer, indicating lower resistance during lithium-ion migration. Bader charge analysis shows that the charges at sites 1, 3, and 6 in $TiO_2@Co_3O_4$ are 0.846+, 0.854+, and 0.863+, respectively, compared to 0.855+, 0.853+, and 0.869+ in TiO_2. The higher electron loss at site 1 of $TiO_2@Co_3O_4$ suggests stronger charge transfer at this site. Due to the bonding state of Ti–O and Co–O at the composite interface (with ICOHP values of −1.406 and −1.330, respectively), charges transfer from TiO_2 and Co_3O_4 to the interface (Fig. 5a). At this stage, the surface Ti atoms exhibit charges of 2.29+, higher than the 2.24+ observed in TiO_2. This indicates that Ti atoms at the interface are in a higher oxidation state, which enhances their binding to surrounding electrons and reduces the binding of lithium ions, facilitating lithium-ion migration and lowering electrode impedance.

4 Conclusions

In this study, $TiO_2@Co_3O_4$ composite microspheres were successfully synthesized *via* a homogeneous precipitation method. Co_3O_4 was uniformly coated on the TiO_2 surface, forming lychee-shaped microspheres with good dispersibility, where Co_3O_4 accounted for 34.99% of the microsphere surface, and focused on understanding the synergistic effects between TiO_2 and Co_3O_4. XRD and Raman spectroscopy analyses confirmed that the material consists of anatase TiO_2 and spinel Co_3O_4. After 100 cycles at a current density of 0.2 C, the specific capacity of the composite reached 482 mA h g^{-1}, representing a 228.8% improvement over the capacity of pure TiO_2 anodes. After 500 cycles at 2C, the discharge-specific capacity of $TiO_2@Co_3O_4$ remained at 385.64 mA h g^{-1}, with a capacity retention rate of 64.46%.

Ex situ characterization of the electrode materials after 100 cycles, where the specific capacity had stabilized, reveals that the active components exist in the form of TiO_2, metallic Co, and CoO. In contrast to the layered distribution observed prior to cycling, Co is redistributed in the form of nanoscale CoO and metallic Co particles dispersed across the TiO_2 matrix after cycling. XPS measurements combined with DFT calculations show that the binding energies of both Ti and Co increase significantly upon formation of the $TiO_2@Co_3O_4$ heterostructure. This suggests that interfacial electron accumulation elevates the oxidation states of the transition metals. The higher oxidation states enhance the electrostatic binding of surrounding electrons, thereby reducing the electrostatic drag on lithium-ion migration, improving ionic mobility, and lowering internal resistance.

5 Experiment and computational details

5.1 Preparation of TiO_2 microsphere precursors

TiO_2 microspheres were synthesized using a modified low-temperature Stöber method.[55] Tetrabutyl titanate (TBOT) was used as the titanium source, and anhydrous ethanol served as

the solvent. A solution of 2 mL 0.01 mol L^{-1} KCl in 400 mL anhydrous ethanol was added to a low-temperature reaction tank and stirred for 1 h using a cryogenic circulating pump to reduce the temperature. When the temperature reached −13 °C, 16 mL TBOT was rapidly added and stirred for 5 min to ensure uniform mixing. The mixture was then allowed to stand at low temperature for 4 h. The precipitate was collected *via* centrifugation and alternately washed three times with anhydrous ethanol and deionized water. Finally, the amorphous TiO_2 microspheres were obtained through freeze-drying and calcined at 600 °C for 2 h at a heating rate of 5 °C min^{-1} to produce anatase-phase TiO_2. The details of the reagents used in the preparation process are provided in the supporting materials (Table S1).

5.2 Preparation of TiO_2@Co_3O_4 microspheres

To prepare TiO_2@Co_3O_4 microspheres, 0.32 g of TiO_2 microspheres, 0.712 g ammonium bicarbonate (NH_4HCO_3), and 100 mL deionized water were added to Beaker A and ultrasonically dispersed for 30 min. Meanwhile, 0.4758 g cobalt(II) chloride hexahydrate ($CoCl_2 \cdot 6H_2O$) was dissolved in 100 mL deionized water in Beaker B, followed by the addition of 0.2424 g urea. The solution in Beaker B was stirred with a glass rod until completely dissolved. After ultrasonic dispersion of the solution in Beaker A was completed, the solution from Beaker B was slowly poured into Beaker A under magnetic stirring for 30 min. The mixture was then heated and stirred in a water bath at 60 °C for 10 h. After the reaction, the product was collected *via* centrifugation and washed alternately three times with deionized water and ethanol. The washed product was dried in an oven at 80 °C and then calcined at 850 °C for 4 h to produce TiO_2@Co_3O_4 microspheres. The thermal decomposition of basic cobalt carbonate[38] follows the reactions:

$$Co^{2+} + OH^- + CO_3^{2-} + H_2O \rightarrow Co_6(OH)_x(CO_3)_y \cdot zH_2O \quad (5)$$

$$Co_6(OH)_x(CO_3)_y \cdot zH_2O \rightarrow Co_6(OH)_x(CO_3)_y + H_2O\uparrow \quad (6)$$

$$Co_6(OH)_x(CO_3)_y + O_2 \rightarrow Co_3O_4 + CO_2\uparrow + H_2O\uparrow \quad (7)$$

5.3 Structural analysis and characterization

The crystal structure of the samples was analyzed using an X-ray powder diffractometer (XRD, PANalytical, Netherlands) with a Cu target, operating at 40 kV and 40 mA. Raman spectroscopy (XploRA, Horiba) was employed to characterize the structural features of the samples, utilizing a laser with a wavelength of 532 nm and a frequency range of 50 cm^{-1} to 1200 cm^{-1}. The chemical composition and atomic structure of the samples were examined using an X-ray photoelectron spectrometer (PHI5000 VersaProbe III, ULVAC-PHI). The sample morphology and energy-dispersive X-ray spectroscopy (EDS) measurements were conducted using a scanning electron microscope (SEM, JSM-5800, JEOL, Japan). High-resolution transmission electron microscopy (HRTEM) was performed using a Thermo Scientific Talos F200X microscope operated at an accelerating voltage of 200 kV. X-ray Photoelectron Spectroscopy (XPS) measurements were carried out using a PHI 5000 VersaProbe I spectrometer equipped with a monochromatic Al Kα X-ray source.

5.4 Electrode preparation and electrochemical performance testing

The active material, Super P carbon black, and polyvinylidene fluoride (PVDF) were weighed in a mass ratio of 7 : 2 : 1 and thoroughly mixed and ground in an agate mortar. The resulting mixture was transferred to a beaker, and an appropriate amount of *N*-methyl-2-pyrrolidone (NMP) was added. The solution was magnetically stirred until a viscous slurry was obtained. The slurry was evenly coated onto copper foil using a blade with a 20 μm gap to form electrode sheets, which were dried at 80 °C for 12 h. Circular electrodes with a diameter of 15 mm were then punched out. A 1 M $LiPF_6$ solution in a solvent mixture of ethylene carbonate (EC), dimethyl carbonate (DMC), and ethyl methyl carbonate (EMC) (vol% = 1 : 1 : 1) was used as the electrolyte. Polypropylene membranes (Celgard 2500) were used as the separator, and lithium metal served as both the counter electrode and the reference electrode. The CR2032 coin cells were assembled in an argon-filled glovebox. Galvanostatic charge–discharge testing (voltage range: 0.01 V to 3.5 V *vs.* Li^+/Li) was conducted using a LAND battery testing system (Land CT2001A). Cyclic voltammetry (CV, scan rate: 0.1 mV s^{-1}) and electrochemical impedance spectroscopy (frequency range: 10^{-2} Hz to 10^6 Hz) were performed using an electrochemical workstation (CS350M).

5.5 DFT simulation

Self-consistent density functional theory (DFT) calculations were carried out using the Vienna *Ab initio* Simulation Package (VASP).[56–58] The revised Perdew–Burke–Ernzerhof functional for solids (PBEsol)[59] within the generalized gradient approximation (GGA) was employed. The plane-wave cutoff energy was set to 450 eV, and the total energy was minimized until the energy difference between successive electronic iterations was less than 10^{-6} eV. Structural relaxation continued until all forces were reduced to below 0.1 eV $Å^{-1}$. The GGA + U method was applied[60] with *U* values of 2.5 eV for Ti[61,62] and 3.0 eV for Co.[63,64] The explicitly treated electrons included: $3p^6 4s^2 4d^2$ (Ti), $3d^7 4s^2$ (Co), $2s^2 2p^4$ (O), and $1s^2 2\ s^1$ (Li). The initial magnetic moments were set to 0 for Co^{3+} and 3.00 μ_B for Co^{2+}. Crystal Orbital Hamilton Population (COHP) analysis was performed using the Lobster code.[65] The Bader charge analysis was conducted with the Bader code.[66]

Author contributions

Conceptualization: Yuan Chen, Weiliang Ma; data curation: Hao Li, Weiliang Ma, Li Chen, Yi Yang; formal analysis: Hao Li, Weiliang Ma, Yi Yang; funding acquisition: Yuan Chen, Weiliang Ma; investigation: Yuan Chen, Weiliang Ma; methodology: Yuan Chen, Weiliang Ma, Marie-Christine Record, Pascal Boulet; project administration: Yuan Chen, Weiliang Ma; resources: Weiliang Ma, Yuan Chen, Marie-Christine Record, Pascal

Boulet; software: Weiliang Ma, Marie-Christine Record, Pascal Boulet supervision: Yuan Chen, Weiliang Ma; validation: Hao Li; visualization: Hao Li, Weiliang Ma, Huawei Luo; writing – original draft: Weiliang Ma, Hao Li; writing – review & editing: Yuan Chen, Yi Yang, Jan-Michael Albina, Juan Wang.

Conflicts of interest

There are no conflicts to declare.

Data availability

Data for this article, including XRD, Raman spectrum, VASP inputs, Bader charge analysis, charge–discharge performance, cycling performance, rate performance, CV curves and Nyquist curves are available at [https://github.com/leon-venir/paper_data/blob/main/y25_li_data.zip].

Supplementary information includes additional figures (SEM images, bonding analysis), detailed modelling procedures, and supporting tables of measurement data. See DOI: https://doi.org/10.1039/d5ra04485e.

Acknowledgements

This research was supported by the Joint Funds of the National Natural Science Foundation of Hubei Province (Grant No. 2025AFD136), the Initial Project of Hubei University of Technology (Grant No. GCC2024017) and the Natural Science Foundation of Hubei Province (Grant No. 2020CFB408). High performance computing resources were provided by the SOLEIL cluster hosted by the Hubei University of Technology.

Notes and references

1 A. Sadar, N. Mohammad, M. Amir and A. Haque, *Process Saf. Environ. Prot.*, 2024, **191**, 1024–1034.
2 K. Wu, Y. Zhang, Y. Zeng and J. Yang, *Prog. Chem.*, 2011, **23**, 401–409.
3 T. Kim, W. Song, D.-Y. Son, L. K. Ono and Y. Qi, *J. Mater. Chem. A*, 2019, **7**, 2942–2964.
4 L. Zhang, X. Li, M. Yang and W. Chen, *Energy Storage Mater.*, 2021, **41**, 522–545.
5 R. Khalid, A. Shah, M. Javed and H. Hussain, *RSC Adv.*, 2025, **15**, 15951–15998.
6 S. Gao, E. Abduryim, C. Chen, C. Dong, X. Guan, S. Guo, Y. Kuai, G. Wu, W. Chen and P. Lu, *J. Phys. Chem. C*, 2023, **127**, 14065–14074.
7 Y. Sun, J. Tang, K. Zhang, J. Yuan, J. Li, D.-M. Zhu, K. Ozawa and L.-C. Qin, *Nanoscale*, 2017, **9**, 2585–2595.
8 M. Zhong, J. Yan, H. Wu, W. Shen, J. Zhang, C. Yu, L. Li, Q. Hao, F. Gao, Y. Tian, Y. Huang and S. Guo, *Fuel Process. Technol.*, 2020, **198**, year.
9 T. Li, Y. Cao, Q. Song, L. Peng, X. Qin, W. Lv and F. Kang, *Small*, 2024, 2403057.
10 C. M. Hayner, X. Zhao and H. H. Kung, *Annu. Rev. Chem. Biomol. Eng.*, 2012, **3**, 445–471.
11 Z. Li, Y. Mao, Q. Tian, W. Zhang and L. Yang, *J. Alloys Compd.*, 2019, **784**, 125–133.
12 F. Dou, L. Shi, G. Chen and D. Zhang, *Electrochem. Energy Rev.*, 2019, **2**, 149–198.
13 E. B. Tetteh, D. Valavanis, E. Daviddi, X. Xu, C. Santana Santos, E. Ventosa, D. Martin-Yerga, W. Schuhmann and P. R. Unwin, *Angew. Chem., Int. Ed.*, 2023, **62**, e202214493.
14 D. Su, S. Dou and G. Wang, *Chem. Mater.*, 2015, **27**, 6022–6029.
15 S. Liang, X. Wang, R. Qi, Y.-J. Cheng, Y. Xia, P. Mueller-Buschbaum and X. Hu, *Adv. Funct. Mater.*, 2022, **32**, 2201675.
16 J. Shen, H. Wang, Y. Zhou, N. Ye, G. Li and L. Wang, *RSC Adv.*, 2012, **2**, 9173–9178.
17 U. Farooq, F. Ahmed, S. A. Pervez, S. Rehman, M. A. Pope, M. Fichtner and E. P. L. Roberts, *RSC Adv.*, 2020, **10**, 29975–29982.
18 W. Liao, Z. Shan and J. Tian, *Trans. Tianjin Univ.*, 2020, **26**, 3–12.
19 J. Guo, J. Li, Y. Huang, M. Zeng and R. Peng, *Mater. Lett.*, 2016, **181**, 289–291.
20 G. S. Zakharova, A. Ottmann, L. Moeller, E. I. Andreikov, Z. A. Fattakhova, I. S. Puzyrev, Q. Zhu, E. Thauer and R. Klingeler, *J. Mater. Sci.*, 2018, **53**, 12244–12253.
21 X. Yan, Z. Wang, M. He, Z. Hou, T. Xia, G. Liu and X. Chen, *Energy Technol.*, 2015, **3**, 801–814.
22 W. Wu, J. Liang, S. Ye, Z. Chen, W. Chen, X. Zhao, L. Zheng, Q. Zhang and J. Liu, *EcoEnergy*, 2024, **2**, 169–180.
23 Y. Zhang, Y. Yan, X. Wang, G. Li, D. Deng, L. Jiang, C. Shu and C. Wang, *Chem. - Eur. J.*, 2014, **20**, 6126–6130.
24 K. Zhou, B. Guo, J. Ma, S. Cui, Y. Bao, T. Wang, H. Qiu and D. Jin, *Phys. Chem. Chem. Phys.*, 2024, **26**, 14898–14907.
25 C. Wang, Q. Li, F. Wang, G. Xia, R. Liu, D. Li, N. Li, J. S. Spendelow and G. Wu, *ACS Appl. Mater. Interfaces*, 2014, **6**, 1243–1250.
26 F. Zhao, T. Chen, Y. Zeng, J. Chen, J. Zheng, Y. Liu and G. Han, *J. Mater. Chem. C*, 2024, **12**, 7126–7145.
27 Z. Cao, Y. Yang, J. Qin, J. He and Z. Su, *Small*, 2021, **17**, 2008165.
28 Y.-C. Kuo and J.-Y. Lin, *Electrochim. Acta*, 2014, **142**, 43–50.
29 K. Liu, J. Cui, J. Yin, J. Man, Y. Cui, Z. Wen and J. Sun, *J. Alloys Compd.*, 2018, **765**, 229–235.
30 H. Luo, L. Shen, K. Rui, H. Li and X. Zhang, *J. Alloys Compd.*, 2013, **572**, 37–42.
31 X. Zhu, X. Yang, C. Lv, S. Guo, J. Li, Z. Zheng, H. Zhu and D. Yang, *ACS Appl. Mater. Interfaces*, 2016, **8**, 18815–18821.
32 Z. Yang, G. Du, Z. Guo, X. Yu, Z. Chen, T. Guo and H. Liu, *J. Mater. Chem.*, 2011, **21**, 8591–8596.
33 X. Chen, Y. Huang, K. Zhang, X. Feng and M. Wang, *Electrochim. Acta*, 2018, **259**, 131–142.
34 Q. Xia, W. Xiong, M. Ni, F. Zan and H. Xia, *FlatChem*, 2019, **17**, 100115.
35 C. Wang, L. Wu, H. Wang, W. Zuo, Y. Li and J. Liu, *Adv. Funct. Mater.*, 2015, **25**, 3524–3533.
36 L. Wang, Y. F. Yuan, Y. Q. Zheng, X. T. Zhang, S. M. Yin and S. Y. Guo, *Mater. Lett.*, 2019, **253**, 5–8.
37 F. Zheng, Z. Yin, H. Xia and Y. Zhang, *Mater. Lett.*, 2017, **197**, 188–191.

38 Y. Li, K. Shang, W. Zhou, L. Tan, X. Pan, M. Liao, J. Lei and L. Zhao, *Electrochim. Acta*, 2016, **222**, 1642–1649.
39 D. Zhao, Q. Hao and C. Xu, *Electrochim. Acta*, 2016, **211**, 83–91.
40 J. Zhao, *Ceram. Int.*, 2019, **45**, 12251–12255.
41 S. S. El-Deen, A. M. Hashem, A. E. A. Ghany, S. Indris, H. Ehrenberg, A. Mauger and C. M. Julien, *Ionics*, 2018, **24**, 2925–2934.
42 J. Guo, F. Li, J. Sui, H. Zhu and X. Zhang, *Ionics*, 2014, **20**, 1635–1639.
43 X. Zhao, C. Kuang, H. Liu, C. An, M. Wang and T. Mu, *ChemSusChem*, 2024, e202400105.
44 J. Luo, J. Zhang, Z. Guo, Z. Liu, S. Dou, W.-D. Liu, Y. Chen and W. Hu, *Nano Res.*, 2023, (16), 4240–4245.
45 M. J. Boyer, L. Vilčiauskas and G. S. Hwang, *Phys. Chem. Chem. Phys.*, 2016, **18**, 27868–27876.
46 D. Zhao, Q. Hao and C. Xu, *Electrochim. Acta*, 2016, **211**, 83–91.
47 B. Wu, J. Wang, J. Li, W. Lin, H. Hu, F. Wang, S. Zhao, C. Gan and J. Zhao, *Electrochim. Acta*, 2016, **209**, 315–322.
48 B. Zhang, F. Wei, Q. Wu, L. Piao, M. Liu and Z. Jin, *J. Phys. Chem. C*, 2015, **119**, 6094–6100.
49 H. Jin, Z. Cui, W. Zhou, L. Guo and S. Yang, *Sci. China Technol. Sci.*, 2013, **56**, 8–12.
50 Y. Li, X. Liu, D. Ren, H. Hsu, G.-L. Xu, J. Hou, L. Wang, X. Feng, L. Lu, W. Xu, Y. Ren, R. Li, X. He, K. Amine and M. Ouyang, *Nano Energy*, 2020, **71**, 104643.
51 T. Song, H. Chen, Z. Li, Q. Xu, H. Liu, Y. Wang and Y. Xia, *Adv. Funct. Mater.*, 2019, **29**, 1900535.
52 C. Dette, M. A. Perez-Osorio, C. S. Kley, P. Punke, C. E. Patrick, P. Jacobson, F. Giustino, S. J. Jung and K. Kern, *Nano Lett.*, 2014, **14**, 6533–6538.
53 V. Singh, M. Kosa, K. Majhi and D. T. Major, *J. Chem. Theory Comput.*, 2015, **11**, 64–72.
54 Y. Zhang, X. Zhang, Q. Pang and J. Yan, *Nat. Commun.*, 2023, **14**, 6130.
55 Y. Chang, P. He, Z. Wei, Y. Chen, H. Wang, C. Wu, Z. Zhou, H. Huang, E. Kowalska and S. Dong, *Mater. Lett.*, 2020, **268**, year.
56 G. Kresse and J. Hafner, *Phys. Rev. B: Condens. Matter Mater. Phys.*, 1993, **47**, 558–561.
57 G. Kresse and J. Furthmüller, *Comput. Mater. Sci.*, 1996, **6**, 15–50.
58 S. L. Dudarev, G. A. Botton, S. Y. Savrasov, C. J. Humphreys and A. P. Sutton, *Phys. Rev. B: Condens. Matter Mater. Phys.*, 1998, **57**, 1505–1509.
59 J. P. Perdew, A. Ruzsinszky, G. I. Csonka, O. A. Vydrov, G. E. Scuseria, L. A. Constantin, X. Zhou and K. Burke, *Phys. Rev. Lett.*, 2008, **100**, 136406.
60 N. Johari, N. Hamzah, A. Faizal, M. Samat, O. Hassan, A. Ali, M. Yahya and M. Taib, *Mater. Today Proc.*, 2022, **66**, 4061–4067.
61 Z. Hu and H. Metiu, *J. Phys. Chem. C*, 2011, **115**, 5841–5845.
62 N. Johari, N. Hamzah, A. Faizal, M. Samat, O. Hassan, A. Ali, M. Yahya and M. Taib, *Mater. Today Proc.*, 2022, **66**, 4061–4067.
63 S. Kenmoe, D. H. Douma, A. T. Raji, B. M'Passi-Mabiala, T. Götsch, F. Girgsdies, A. Knop-Gericke, R. Schlögl and E. Spohr, *Nanomaterials*, 2022, **12**, 921.
64 M. Jamal, S. Shahriyar Nishat and A. Sharif, *Chem. Phys.*, 2021, **545**, 111160.
65 S. Maintz, V. L. Deringer, A. L. Tchougréeff and R. Dronskowski, *LOBSTER: A Tool to Extract Chemical Bonding from Plane-Wave Based DFT*, 2016.
66 G. Henkelman, A. Arnaldsson and H. Jónsson, *Comput. Mater. Sci.*, 2006, **36**, 354–360.